

Periodic Narrowband Radio Wave Emissions and Inward Plasma Transport at Saturn's Magnetosphere

S. Wing 1 P. C. Brandt J. D. G. Mitchell D. J. R. Johnson W. S. Kurth and J. D. Menietti The Johns Hopkins University, Applied Physics Laboratory, Laurel, MD, USA

Andrews University, Berrien Springs, MI, USA

University of Iowa, Iowa City, IA, USA

Received 2019 November 21; revised 2020 March 18; accepted 2020 March 18; published 2020 May 11

Abstract

The abrupt brightening of an Energetic Neutral Atom (ENA) blob or cloud has been interpreted as plasma injection in the Kronian magnetosphere (termed ENA injection herein). Morphologically, there appears to be two types of abrupt ENA cloud brightening: (1) the brightening of a large cloud usually seen at distances $>10-12\,R_{\rm s}$ ($R_{\rm s}\sim 60,268\,{\rm km}$) in the midnight or postmidnight region; (2) the brightening of a smaller cloud usually seen at distances $<10-12\,R_{\rm s}$ around 21-03 magnetic local time. Among many radio waves observed at Saturn, type 2 ENA injections correlate best with the 5 kHz narrowband (NB) waves. Using Cassini Ion and Neutral Camera (INCA) and Radio and Plasma Wave Science (RPWS) data, we examine the periodicities of the type 2 ENA injections and the 5 kHz NB emissions as well as their cross-correlations, which have been previously used to measure the lag times or phase differences. Because correlational analysis can only establish linear relationships, we also use mutual information to establish linear and nonlinear relationships. On average, the peak of the 5 kHz NB emission lags those of the type 2 ENA injection by about a few minutes to 2 hr. The injection of hot plasma to the inner magnetosphere can lead to temperature anisotropy, which can generate electrostatic upper hybrid waves, which upon encountering the high-density gradient at the outer edge of the Enceladus density torus, can mode convert to Z mode and then to O mode. The 5 kHz NB waves commonly propagate in the O mode.

Unified Astronomy Thesaurus concepts: Magnetospheric radio emissions (998); Space plasmas (1544); Neutral hydrogen clouds (1099); Planetary magnetosphere (997); Magnetohydrodynamics (1964); Lomb-Scargle periodogram (1959); Multi-periodic pulsation (1078)

1. Introduction

An Energetic Neutral Atom (ENA) can be created when a singly charged energetic ion exchanges charge with an ambient neutral atom in the magnetosphere. The resulting ENA would have approximately the same energy as the original ion but now travels unencumbered by the ambient electric and magnetic fields. The Cassini spacecraft regularly observed hot plasma clouds or blobs of ENAs with energies \sim 3 to >220 keV in the Saturn's magnetosphere at about 5–30 Saturn radii (R_s) from the planet (R_s = Saturn radius \sim 60,268 km; Paranicas et al. 2005; Carbary et al. 2008a, 2008b; Carbary & Mitchell 2014). These ENA blobs usually corotate with the planet, although with some angular velocity lag compared with that of the planet. ENA blobs have been observed to wax and wane with periodicity around 11 hr (Carbary et al. 2008a, 2009, 2010), with the peak count (or intensity) occurring on the nightside (Krimigis et al. 2005).

The abrupt brightening of an ENA blob or cloud seen in the Kronian magnetosphere has been interpreted as a plasma injection (termed ENA injection herein; Mitchell et al. 2015). Mitchell et al. (2015) suggested that there are two types of plasma injections in the Kronian magnetosphere: (1) injections that are associated with the nightside reconnection and current sheet collapse and are usually seen at distances $>10-12\,R_{\rm s}$ in the midnight or postmidnight region; and (2) injections that are associated with interchange instability and are usually seen at distances $<10-12\,R_{\rm s}$ around midnight, 21–03 magnetic local time (MLT; see also Azari et al. 2018). However, as they pointed out, this classification of injections is not always clear. Type 1 injections, which result from reconnection, may also

move planetward due to flux tube interchange as commonly interpreted in the terrestrial magnetosphere (e.g., Birn et al. 2009; Johnson & Wing 2009; Wing & Johnson 2009, 2010; Wolf et al. 2009). However, Mitchell et al. (2015) argued that in the type 1 injection, after the reconnection, the current sheet collapses and a cross-tail electric field develops, which can nonadiabatically heat, accelerate, and transport plasma via $E \times B$ inward, whereas in type 2 injection, the primary force in the inward transport is the buoyancy force, and the field-line tension and the already heated plasma would be heated adiabatically. The two types of injections can be causally interrelated (Mitchell et al. 2015). In their scenario, reconnection and the subsequent current sheet collapse will return hot tenuous flux tubes toward the planet, which would subsequently become buoyantly unstable and undergo flux tube interchange. In another aspect of that scenario, the flux tube interchange in the inner or middle magnetosphere would facilitate the transport of cold plasma outward and load the outer magnetosphere with plasma, leading to the next episode of the stretched field lines and reconnection.

An example of ENA brightening for types 1 and 2 is shown in Figure 1. Other examples of type 1 ENA brightenings or injections can be found in Mitchell et al. (2005, 2009, 2015), and other examples of type 2 can be found in Mitchell et al. (2015) and Radioti et al. (2013). The in situ plasma observations have also revealed the two types of injections with similar characteristics (Chen & Hill 2008; Thomsen 2013; Achilleos et al. 2015; Thomsen et al. 2015); although, the ENA images do not resolve the small injections that can be detected in the plasma data. The earlier in situ studies did not distinguish the two types of injections. Recently, Azari et al. (2018)

Type 1 and Type 2 ENA injections

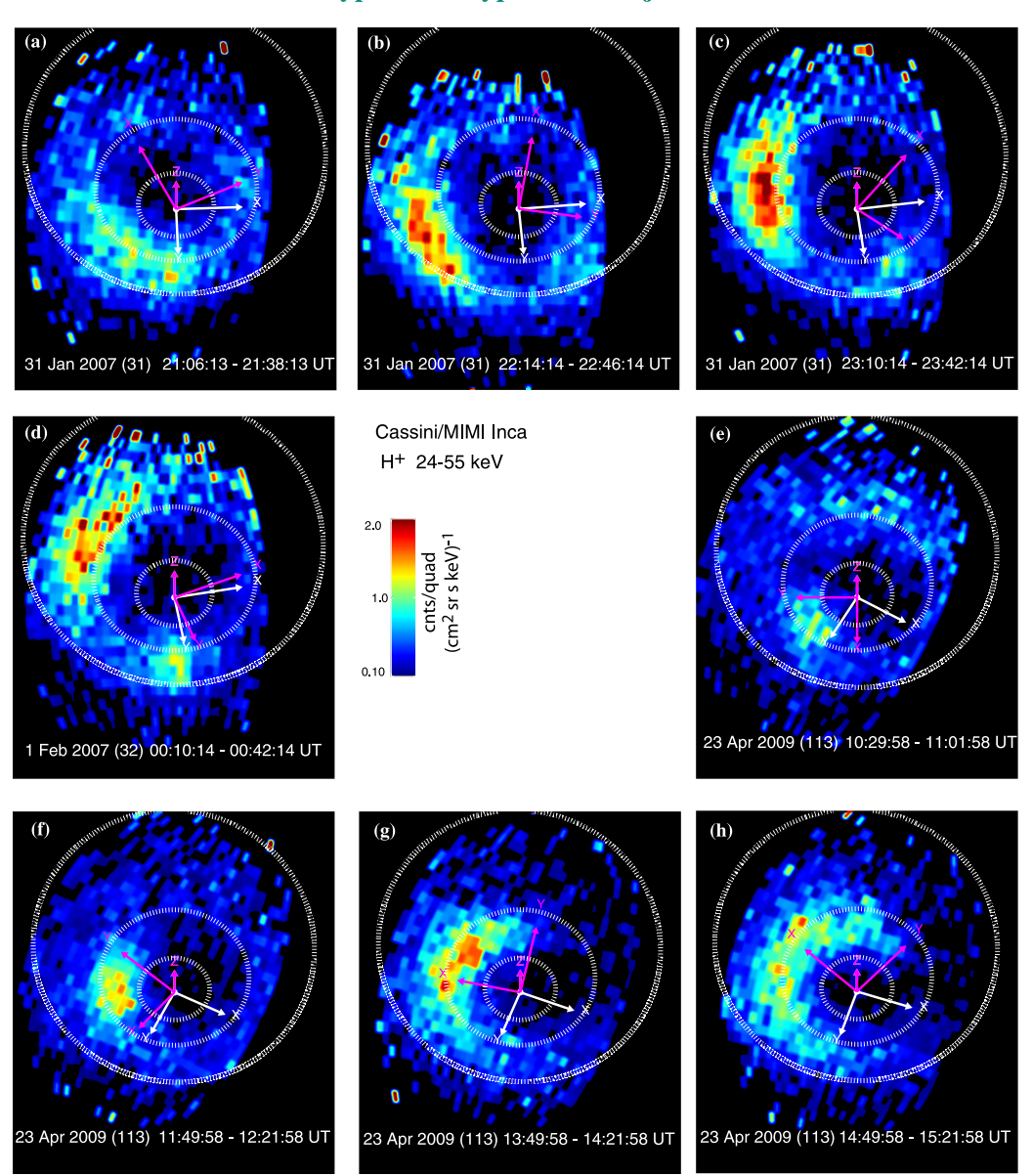


Figure 1. Examples of ENA type 1 injection on 2007 January 31 and type 2 injections on 2009 April 23. Panels (a)—(d) show the evolution of type 1 injection while the panels (e)—(h) show the evolution of type 2 injection. Each panel shows the intensity of the H 24–55 keV ENA as observed by the Cassini MIMI INCA imager. The X (sunward) and Y (duskward) axes in SZS coordinate are depicted by the white arrows while the X, Y, and Z (northward) axes in SKR longitudinal coordinate system are depicted by the magenta arrows (Kurth et al. 2007). Saturn is represented by a little white disk. The three dotted circles represent the orbits of Enceladus $(4.0 R_s)$, Rhea $(9.1 R_s)$, and Titan $(21 R_s)$. The images are averaged over eight frames, and each frame is about 4 minutes. The color represents the flux in units (atoms cm² sr s keV)⁻¹. In the type 1 injection, the bright blob extends from the orbit of Rhea to beyond Titan, while in the type 2 injection, the bright blob appears between the orbit of Rhea and Enceladus.

reported that, statistically, the interchange injections, which would correspond to type 2 ENA brightening, can be found at $5 R_s < r < 11 R_s$ and primarily between 21 and 03 local time.

Planetary magnetospheres, including the Kronian magnetosphere, emit radio waves. Some of the strongest emissions are associated with the electron cyclotron maser instability (Wu & Lee 1979; Lamy et al. 2010). The Auroral Kilometric radiation (AKR) at Earth is an example of such radio emission (Gurnett 1974). The corresponding emission at Saturn is known as Saturn Kilometric Radiation (SKR), which has frequencies ranging from $\sim \! 10$ to $\sim \! 1500$ kHz (Lamy et al. 2008; Kurth et al. 2009). In addition to SKR, the Kronian magnetosphere also emits numerous weaker radio wave emissions at lower

frequencies with narrow bandwidth, which are commonly known as narrowband (NB) emissions (Gurnett et al. 1981). The 5 kHz (e.g., Wang et al. 2010), 10 kHz (e.g., Menietti et al. 2009), and 20–30 kHz (e.g., Ye et al. 2009) emissions are examples of such NB emissions. Figure 2 shows an example of SKR and various NB emissions, including the 5 kHz NB, over a period of 2 days, on 2009 April 22–23. The present study focuses on the 5 kHz NB because the type 2 ENA injections correlate best with the 5 kHz NB emissions, as described in Section 5.

The SKR has been causally associated with ENA type 1 injections (Mitchell et al. 2015) and has been associated with upward field-aligned currents (FACs) and electron cyclotron

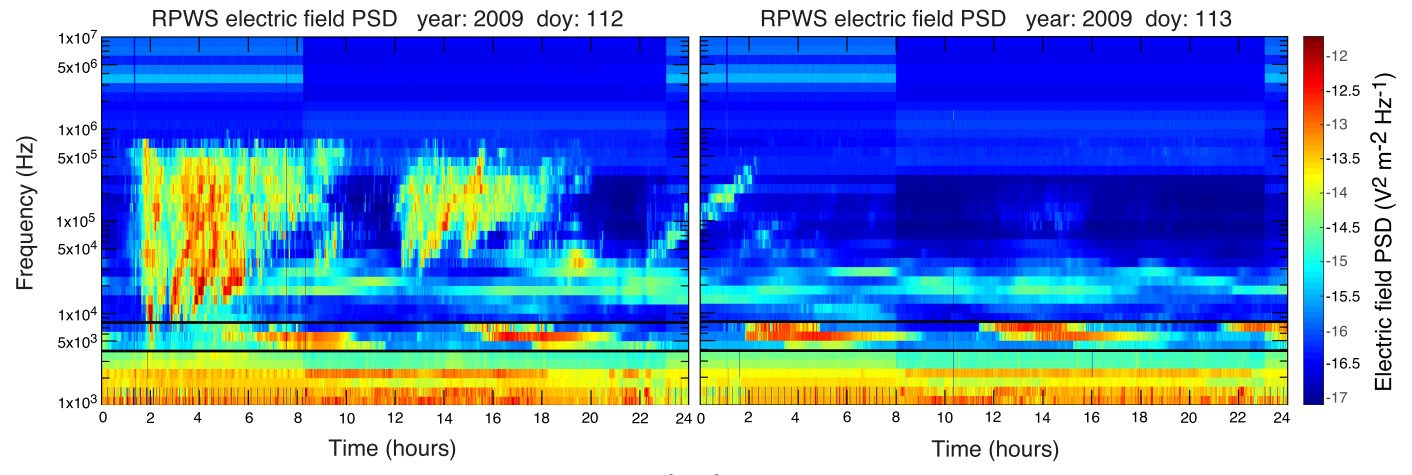


Figure 2. An example of the electric field power spectral density (PSD; V^2 m⁻² Hz) obtained from Cassini RPWS for 2009 April 22–23 (doy 112–113). The spectrogram shows various wave emissions at different frequencies such as SKR (\sim 15–1000 kHz), and NBs at 20–30, 10, and 5 kHz. The 5 kHz NB can be seen between the two horizontal black lines.

maser instability (Ergun et al. 2000; Lamy et al. 2010, 2013; Jackman et al. 2013; Bradley et al. 2018). One scenario that can link plasma injections and SKR is that the plasma pressure inside the injected flux tube (bubble) may be smaller than that outside the flux tube. This pressure gradient can generate upward and downward FACs (Nakamura et al. 2001; Sergeev et al. 2004; Wing et al. 2014). The upward field-aligned electric field that arises in the upward FAC region can accelerate electrons, leading to the cyclotron maser radiation (Ergun et al. 2000).

Unlike SKR, which is thought to be a direct radiation from electron cyclotron maser instability, the NB emissions, including the 5 kHz NB, are mode converted from other waves. However, there has not been a clear consensus as to which waves they convert from and how these waves get generated in the first place. The 5 kHz NB emission has been identified as the ordinary (O) mode emission (Ye et al. 2009). Some studies suggested that a loss cone distribution via cyclotron maser instability can generate Z-mode waves, which can then mode convert to ordinary (O) mode in the presence of a density gradient (Menietti et al. 2009; Ye et al. 2010b). Ye et al. (2009) suggested that the 5 kHz NB waves are mode converted from the electrostatic upper hybrid waves according to linear or/and nonlinear mode conversion theory (Melrose 1981; Jones 1988; Horne 1989, 1990); although, the origin of the upper hybrid mode is not clear. Ye et al. (2010a) suggested that an enhanced partial ring current perturbs the magnetosphere and triggers the enhancement of the NB emissions. More recently, Menietti et al. (2016) surveyed Cassini Radio and Plasma Wave Science (RPWS) observations and concluded that Z-mode waves are driven by an electron temperature anisotropy near the equator at the outer edge of the Enceladus density torus. The Enceladus plasma or density torus is nominally located between 3 and $5R_s$ but can extend from 2 and $8R_s$, depending on the species (Johnson et al. 2006; Persoon et al. 2013).

Wang et al. (2010) examined 23 events in which the 5 kHz NB emissions are observed by Cassini RPWS, and Ion and Neutral Camera (INCA) data are available. Excluding the one event in which INCA does not point to Saturn the whole time, all NB events have accompanying ENA hot plasma clouds. However, only 5 out of the 23 events show simultaneous intensifications of ENA hot plasma clouds and 5 kHz NB

emissions. They did not quantify what "simultaneous" means or the precise phase relation between the ENA plasma clouds and the NB, other than stating that there is a strong trend for both to appear on the nightside. They suggested that the rotating hot plasma clouds trigger the NB emissions when they pass through a certain local time. In this scenario, the phase relation between NB and the ENA plasma can be variable, as suggested in their data. A precise phase relation and temporal response time (τ) would allow us to infer the possible causal relationship between the ENA injections and the NB. For example, if the ENA injection leads the NB, then it would allow for a scenario in which the ENA can trigger the NB emission and vice versa. However, Wang et al. (2010) did not distinguish type 1 from type 2 ENA injections and vice versa. At the time of their publication in 2010, the distinction between types 1 and 2 had yet been neither published nor widely known.

The Saturn rotation period has often been estimated from the periodicity of SKR because of the difficulty of estimating the periodicity from tracking a surface feature on a gas planet (e.g., Azari et al. 2019). The intensity of SKR has been observed to have periodicity of ~10.8 hr (e.g., Davies et al. 1995; Gurnett et al. 2005). It turns out that many phenomena including magnetic field, plasma density, and pressure variations in the middle and inner magnetosphere also exhibit periodicities with similar periods as SKR (Bradley et al. 2018). Carbary et al. (2008a) investigated the periodicity of ENA injections and found that the 20-50 keV hydrogen (H) and 64-144 keV oxygen (O) ENA injections have periodicities of 11.7 \pm 2.4 hr and $10.8 \pm 0.2 \, hr$, respectively. However, Carbary et al. (2008a) did not distinguish type 1 and 2 ENA injections because the distinction was not known at the time the study was conducted. Thus, it is not clear from this study if the type 1 injections (occurring at $r > 10-12 R_s$) and the type 2 injections (occurring at r < 10–12 R_s) would have the same or different periodicities. Moreover, type 2 injection periodicity would be relevant to the flux tube interchange injection dynamics in the inner magnetosphere (Azari et al. 2019).

In the present study, we examine more closely the relationship between ENA type 2 injection and the 5 kHz NB at high time resolution (5 minutes). We examine the periodicities of the type 2 injections (occurring at r < 10–12 $R_{\rm s}$) and NB waves and their cross-correlations. However, cross-correlations can

Table 1Selected ENA Type 2 Injection Events

Event Number	Start Time	End Time	Comment
1	2007 038 22:45:00	2007 039 17:25:00	•••
2	2007 042 02:00:00	2007 043 01:00:00	NB contaminated by SKR
3	2007 096 00:15:00	2007 096 17:22:00	
4	2008 025 14:30:00	2008 026 04:00:00	weak NB
5	2008 078 11:00:00	2008 079 21:00:00	weak NB
6	2009 012 12:45:00	2009 013 12:09:30	•••
7	2009 021 14:30:00	2009 023 13:45:00	•••
8	2009 065 06:00:00	2009 066 04:00:00	Two injections simultaneously
9	2009 112 22:20:00	2009 114 18:00:00	
10	2009 149 02:00:00	2009 149 16:00:00	•••
11	2009 151 00:00:00	2009 152 07:00:00	•••
12	2009 179 02:00:00	2009 179 17:51:00	
13	2009 181 00:00:00	2009 181 18:30:00	weak NB

Note. Five of the events are excluded from the analysis for the reasons mentioned in the comment column.

only establish a linear relationship. Hence, we supplement cross-correlation with mutual information (MI) (Li 1990; Darbellay & Vajda 1999; Tsonis 2001), which can establish linear and nonlinear relationship between two variables.

2. Data Set and Data Treatment

The Cassini spacecraft was launched in 1997 and entered Saturn's orbit in 2004. The present study uses observations from Magnetospheric Imaging Instrument (MIMI; Krimigis et al. 2004) and RPWS (Gurnett et al. 2004) instruments on board Cassini. The MIMI instrument suite includes the INCA instrument that can observe ENAs in the energy range \sim 7–200 keV nuc⁻¹ (Krimigis et al. 2004). INCA has a field of view of $120^{\circ} \times 90^{\circ}$ with spatial resolution of 64×64 , 32×32 , or 16×16 pixels, depending on the energy resolution selected. For the present study, we select ENA H with energy range 55–90 keV, which typically has 2D spatial resolution of 32×32 pixels and time resolution of 4 minutes. We impose a restriction that the spacecraft has to be at latitudes between 35° and 75°, in order to get a favorable global viewing angle of the equatorial plane where most of the ENAs come from. Restricting the viewing to latitudes >35° is also better for detecting the 5 kHz NB because the dense plasma torus may limit the wave propagation through the equatorial region (Wang et al. 2010). We use the standard MIMI data processing software to process the INCA data (http://cassini-mimi.jhuapl.edu/PDS_ HigherOrder/uncompressed/MIMI_AnalysisUserGuide12.pdf). The ENA count rate in each image is converted to ENA intensity (atoms cm⁻² s⁻¹ sr⁻¹ keV⁻¹), and then the image is projected onto the equatorial plane, taking into account the cosine factor due to the slanted geometric viewing (e.g., Carbary et al. 2008b). The equatorial projection is done in Saturn Equatorial system (SZS) coordinate system (Z is parallel to the Saturn spin axis, X is sunward, and $Y = Z \times X$). Then, we construct a running 30 minute window average from which keograms for MLT = 21-03 hr are constructed at 5 minutes time resolution. The keogram method is a method whereby a slice of the 2D image at certain MLT range is plotted versus time. This method has been used extensively in the study of ultraviolet images of the Earth's aurorae (Eather 1984; Rairden & Mende 1989) and more recently ENA images of Saturn's magnetosphere (Carbary et al. 2009; Carbary & Mitchell 2014). From the keograms, we integrate the ENA fluxes over the radial distance between 5 and $9R_s$, where type 2 injections are

expected. The periodicity of the ENA intensity is obtained from the Lomb–Scargle PSD. This method is similar to that used in Carbary et al. (2010).

Note that although the 24–55 keV H atoms are typically observed by INCA with higher count rates than the 55–90 keV H atoms, for the present study, we choose the latter because the 24–55 keV particles are more persistent with corotation. Hence, if we are interested in the periodicity of the injection, then the 55–90 keV particles may be a better choice.

The Cassini RPWS measures oscillating electric fields in the range 1 Hz-16 MHz and magnetic fields in the range 1 Hz-12 kHz (Gurnett et al. 2004). The 5 kHz NB emissions used in the present study are measured by the RPWS High-Frequency Receiver (HFR) covering 3.5 kHz to 16 MHz and Medium-Frequency Receiver covering 24 Hz–12 kHz (mainly by HFR). The 5 kHz NB emission has a bandwidth of 1-3 kHz (Menietti et al. 2009; Wang et al. 2010), and hence, we use the frequency range of 3.9-6.3 kHz. The quantity that we use from RPWS HFR observations is the electric field PSD ($V^2 \text{ m}^{-2} \text{Hz}$; measured intensity divided by the square of the antenna length) at one minute resolution (Ye et al. 2010a). The electric field PSD integrated from 3.9 to 6.3 kHz (three frequencies in RPWS: 3.9, 5.0, and 6.3 kHz) is then averaged with a 5 minute window running average. The periodicity is obtained from the Lomb-Scargle PSD.

We search for type 2 injection events during the period 2007–2009 when the spacecraft is located at latitudes between 35° and 75°. We find there are 13 events that have good type 2 injections and good RPWS data (as determined by the instrument teams). Table 1 lists the 13 events. Three of these events have weak NB emissions, i.e., events having electric field PSD $\lesssim 10^{-14}~({\rm V^2~m^{-2}~Hz})$. The weak NB events show much weaker cross-correlations between the ENA and NB emissions than those for stronger NB emissions. In one event, two injections appear simultaneously, which complicates the determination of the periodicity. In another event, the 5 kHz NB emission is contaminated by SKR that extends to lower frequencies. Thus, out of the 13 events, eight events are deemed good for this study.

3. Three Examples of Simultaneous ENA Injections and NB Emissions

As mentioned above, 13 events are selected in which there are simultaneous type 2 ENA injections and RPWS wave

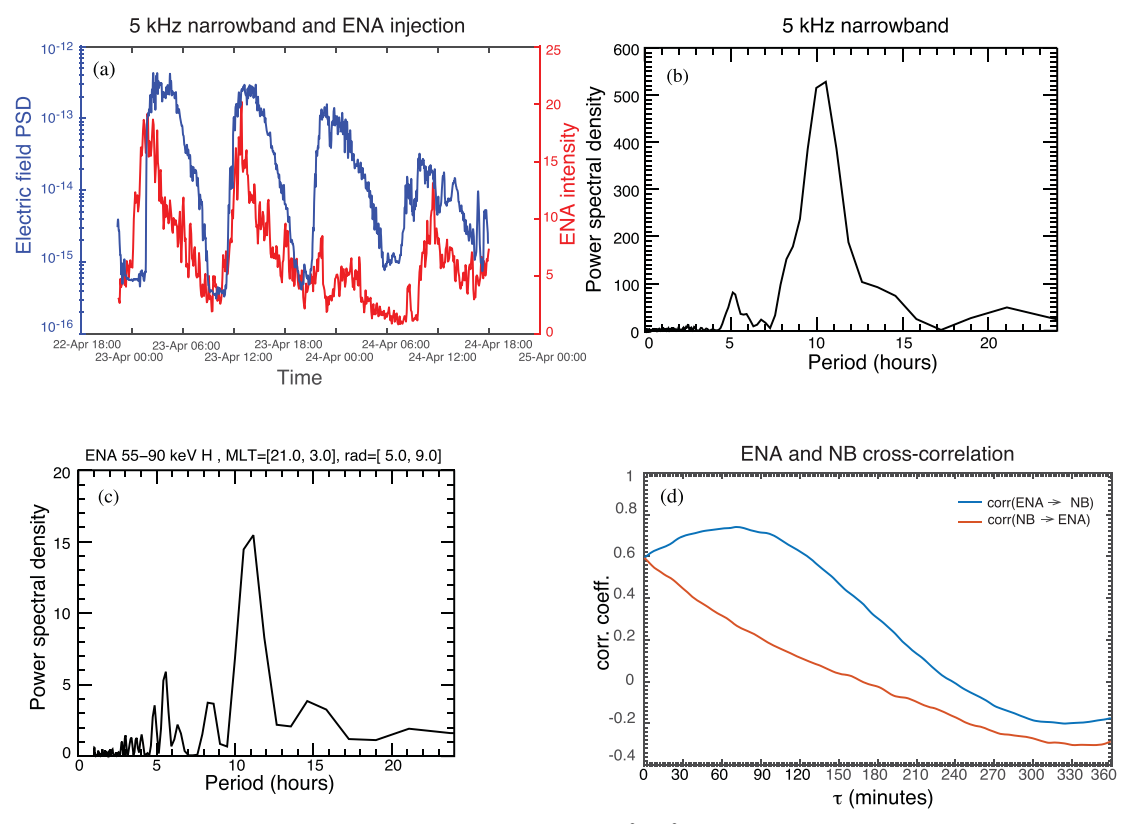


Figure 3. 2009 April 22 (doy 112) event. Panel (a): time series of the electric field PSD (V^2 m⁻² Hz) of the 5 kHz NB emission (blue curve) and type 2 ENA intensity integrated over 21–03 MLT and 5–9 R_s (atoms cm² sr s keV)⁻¹ (red curve). Panel (b): Lomb–Scargle periodogram of the 5 kHz NB (blue curve in panel (a)) showing a peak at 10–11 hr. Panel (c): Lomb–Scargle periodogram of the ENA intensity time series (red curve in panel (a)) showing a peak at 10–11 hr. Panel (d): time-shifted correlations: corr(ENA(t), NB(t + τ)) (ENA \to NB, blue curve) and corr(ENA(t) + τ), NB(t) (NB \to ENA, red curve).

observations. Out of the 13 events, eight are suitable for further analysis. In general, one can see that type 2 ENA and the 5 kHz NB emissions peak nearly simultaneously, but there is some variability. We select three examples to illustrate the variability.

3.1. 2009 April 22 Event

Figure 3 presents an event from 2009 April 22–24 (event #9 in Table 1). In Figure 3(a), the blue curve shows the time series of the electric field PSD of the 5 kHz NB (actually integrated from 3.9 to 6.3 kHz). The red curve shows the ENA intensity integrated over 21–03 MLT and 5–9 $R_{\rm s}$. Both curves show cyclical behavior. Figure 3(b) is a Lomb–Scargle periodogram of the NB (blue) curve in Figure 3(a), showing a peak between 10 and 11 hr. Figure 3(c) shows the periodogram of the ENA (red) curve in Figure 3(a). This periodogram also peaks between 10 and 11 hr.

In Figure 3(a), the ENA peak generally leads the NB peak, but the lead time varies or may even vanish. In the first two NB peaks, it is clear that ENA leads NB intensifications by a few hours; but in the subsequent peaks, the lead time seems to have diminished. The third NB peak corresponds to a double peak in the ENA curve. The first ENA peak leads the NB peak, but the second ENA peak seems to lag the NB peak. In order to get an overall sense of the lead or lag time, time-shifted cross-correlations are performed. In Figure 3(d), the blue curve shows corr(ENA(t), NB($t + \tau$)) (shorthanded as ENA \rightarrow NB) while the red curve shows corr(ENA($t + \tau$), NB(t)) (shorthanded as NB \rightarrow ENA). By definition, the blue and the red curves meet at t = 0, but for larger τ , the blue curve is generally higher than the red curve. The blue curve peaks at correlation coefficient (t) = 0.74 while the

red curve peaks at r=0.59. The peaks are significant at p<0.01 (the probability of two random variables giving a correlation coefficient as large as r is <0.01). The blue curve peaks at $\sim60-120$ minutes, suggesting that the NB emission lags ENA injections by about 1-2 hr.

3.2. 2009 January 21 Event

Figure 4 presents the 2009 January 21–23 event (event #7 in Table 1) in the same format as Figure 3. The Lomb–Scargle periodogram for the NB shows a peak between 11 and 12 hr (Figure 4(b)) while that for ENA also shows a peak between 11 and 12 hr (Figure 4(c)). As can be seen in Figure 4(a), the peaks of the ENA and NB curves are much closer together than those in the 2009 April 22 event shown in Figure 3(a). The time-shifted cross-correlation shows that corr(ENA(t), NB(t + τ)) (blue curve) is slightly larger than corr(ENA(t + τ), NB(t)) (red curve), and both curves peak near $\tau \sim 0$ minute with t = 0.62, which is significant at t < 0.01.

3.3. 2009 May 31 Event

Figure 5 presents the 2009 May 31–June 1 event (event #11 in Table 1) in the same format as Figure 3. The Lomb–Scargle periodogram for the NB shows a peak around 10–11 hr (Figure 5(b)) while that for ENA shows a peak at \sim 12 hr (Figure 5(c)). This example is picked to show that not all events are as clear as the first two events shown above. Figure 5(a) shows that in the first cycle, NB peaks initially lag ENA peaks by a short time. So, this is similar to the 2009 April 22 event. However, at the following cycle, the ENA curve only has a

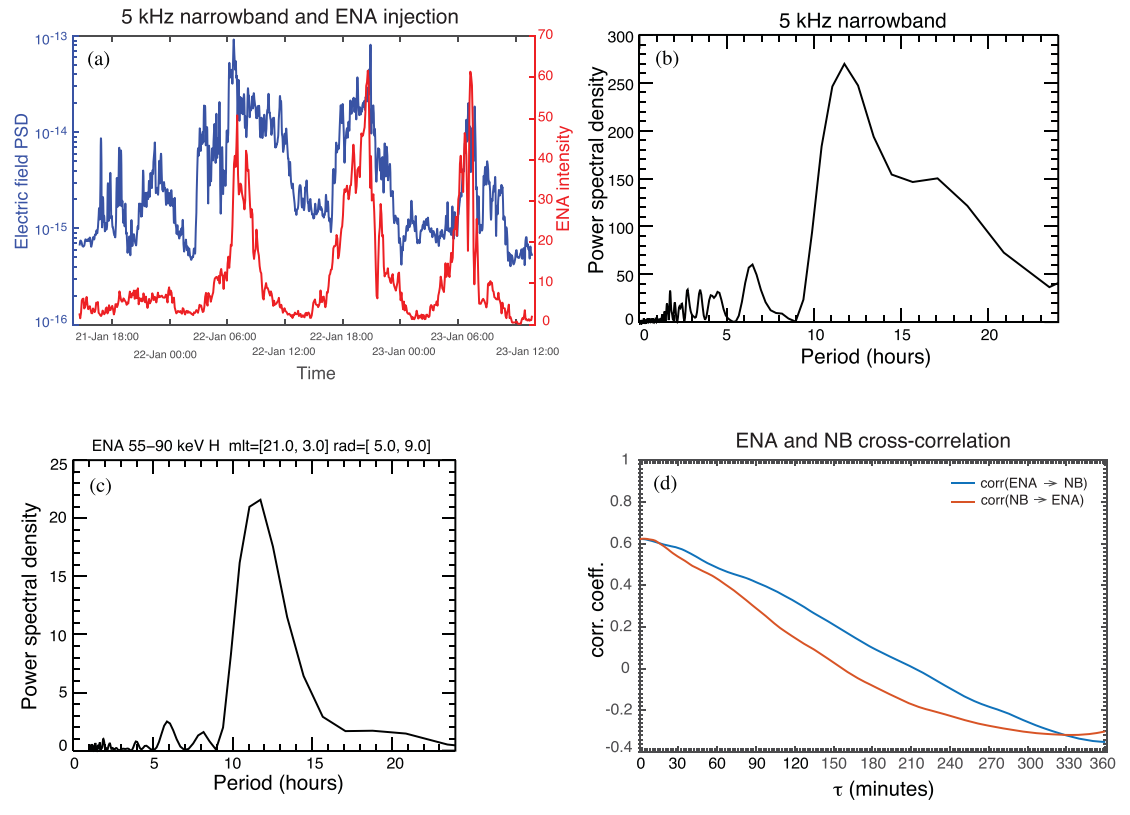


Figure 4. 2009 January 21(doy 21) event. Panel (a): time series of the electric field PSD (V^2 m⁻² Hz) of the 5 kHz NB emission (blue curve) and type 2 ENA intensity integrated over 21–03 MLT and 5–9 R_s (atoms cm² sr s keV)⁻¹ (red curve). Panel (b): Lomb–Scargle periodogram of the 5 kHz NB (blue curve in panel (a)) showing a peak at 11–12 hr. Panel (c): Lomb–Scargle periodogram of the ENA intensity time series (red curve in panel (a)) showing a peak at 11–12 hr. Panel (d): time-shifted correlations: corr(ENA(t), NB(t + τ)) (ENA \to NB, blue curve) and corr(ENA(t + τ), NB(t)) (NB \to ENA, red curve).

small peak, and the NB curve has a double peak. The ENA peak lags the first peak and leads the second peak. At the next cycle, the third cycle, the situation is reversed. The ENA has a double peak while the NB has a single peak. The NB peak lags the first ENA peak and leads the second ENA peak. Figure 5(d) shows that corr(ENA(t), NB($t+\tau$)) (blue curve) has a broad peak $\tau \sim 60$ –140 minutes and corr(ENA($t+\tau$), NB(t)) (red curve) has a broad peak at $\tau \sim 0$ –30 minutes. As in the previous examples, the blue curve is generally larger than the red curve, suggesting that the correlation is better for when NB lags ENA instead of the other way around. Both the blue and the red curves peak at t=0.27 and t=0.26, respectively. Due to the large number of points (t=0.26), the correlations are significant at t=0.01.

4. Ensemble Cross-correlation, MI, and Periodicities

As demonstrated in Figures 3–5, there is some variability in the ENA and NB periodicities and their phase relations. In most cases, the ENA peaks lead the NB peaks; but in a few cases, it is the other way around. However, in all eight selected cases, the ENA and NB peaks are simultaneous within a 2 hr window.

One can get a sense of the ensemble average of the eight events by stringing the eight time series from these eight events into one large time series with data gaps between events. We then calculate the Lomb–Scargle periodograms and the cross-correlation for the ensemble events. Figures 6(a) and (b) plot the periodograms for the NB and ENA intensities, respectively. The curves in both figures have been smoothed with a running window average. Figure 6(a) shows that the ensemble 5 kHz NB has a periodicity of 10–11 hr, while Figure 6(b) shows that

the ensemble type 2 injection has a periodicity of $11-12\,\mathrm{hr}$. Figure 6(c) shows that the ensemble corr(ENA(t), NB($t+\tau$)) (blue curve) peaks at $\tau\sim7\,\mathrm{minutes}$ ($r=0.42;\ p<0.01;\ n=1937$), but the peak is rather broad. The ensemble corr (ENA($t+\tau$), NB(t)) (red curve) peaks at $\tau\sim0\,\mathrm{minutes}$ ($t=0.41;\ p<0.01;\ n=1937$). The blue curve is generally larger than the red curve, suggesting that the correlation is better when the 5 kHz NB emission lags the type 2 ENA injection than the other way around. However, the correlation function gives a measure of linear correlation. If the processes linking the type 2 ENA injections and 5 kHz NB emissions were nonlinear, the correlation function would be inadequate.

MI gives a measure of the linear and nonlinear correlation between the two variables (Li 1990; Darbellay & Vajda 1999; Tsonis 2001). MI has been applied to problems in the magnetospheric and ionospheric physics (e.g., March et al. 2005; De Michelis et al. 2011, 2017; Materassi et al. 2011; Wing et al. 2016; Wing & Johnson 2019).

To capture the linear and nonlinear correlations, we apply time-shifted MI to the ENA and NB time series data. In Figure 7(a), the blue curve shows MI(ENA(t), NB(t) while the red curve shows MI(ENA(t + τ), NB(t) for the 2009 April 22 event. Thus, Figure 7(a) can be compared with Figure 3(d), which shows the time-shifted cross-correlation of the same variables. Figures 7(b) and (c) show the same quantities as Figure 7(a), except that they are for the 2009 January 21 and 2009 May 31 events, respectively. Figure 7(d) shows the time-shifted MI for the ensemble events. Figures 7(b)–(d) can be compared with their cross-correlation counterparts in Figures 4(d), 5(d), and 6(c), respectively.

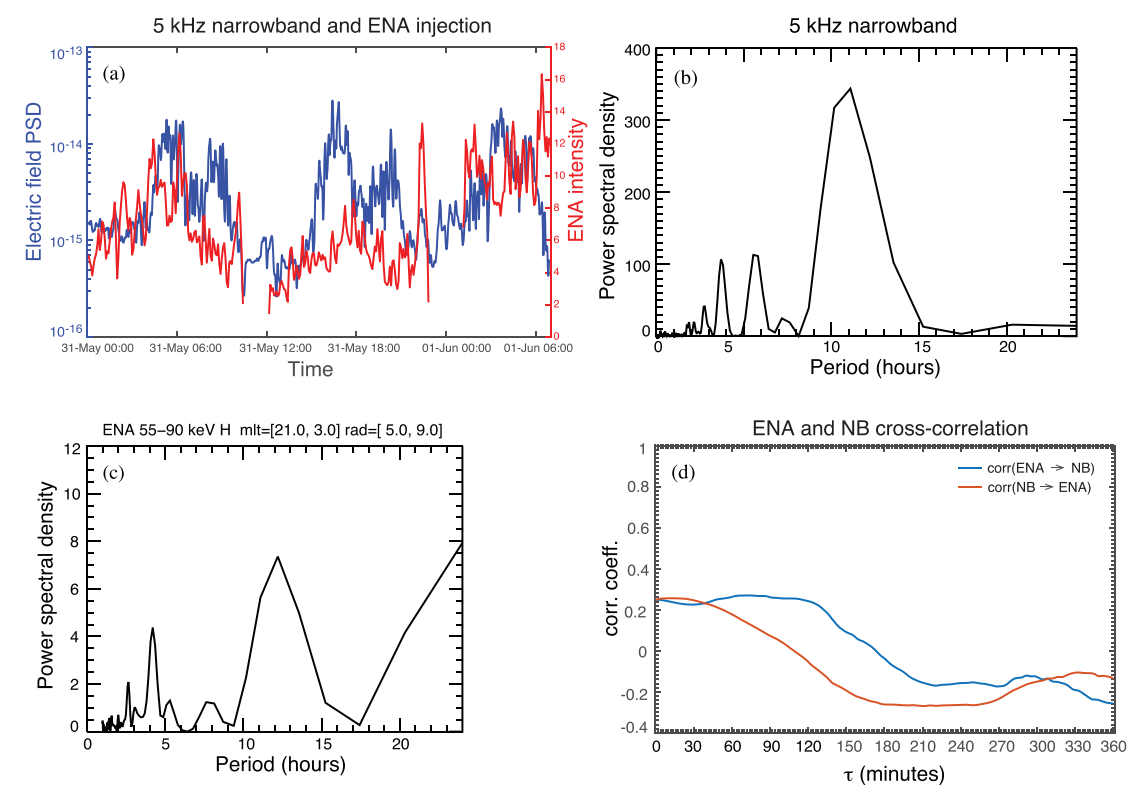


Figure 5. 2009 May 31 (doy 151) event. Panel (a): time series of the electric field PSD (V^2 m⁻² Hz) of the 5 kHz NB emission (blue curve) and type 2 ENA intensity integrated over 21–03 MLT and 5–9 R_s (atoms cm² sr s keV)⁻¹ (red curve). Panel (b): Lomb–Scargle periodogram of the 5 kHz NB (blue curve in panel (a)) showing a peak at 10–11 hr. Panel (c): Lomb–Scargle periodogram of the ENA intensity time series (red curve in panel (a)) showing a peak around 12 hr. Panel (d): time-shifted correlations: corr(ENA(t), NB(t + τ)) (ENA \rightarrow NB, blue curve) and corr(ENA(t + τ), NB(t)) (NB \rightarrow ENA, red curve).

The comparisons show that the inclusion of the nonlinearities changes the nature of the correlations between the ENA injections and NB emissions. There is variability in each event, but in general, MI(ENA(t), NB(t+\tau)) shows a peak at larger τ than that from corr(ENA(t), NB(t+\tau)). This can be seen clearly in the MI and corr for the ensemble events. The blue curve in Figure 7(d) has a broad peak from $\tau\sim$ a few minutes to 2 hr, whereas the blue curve in Figure 6(c) peaks at τ close to 0 minute. The broad peak at $\tau\sim$ a few minutes to 2 hr in the blue curve better captures the variability in the lag times seen in individual events. The peak of the blue curve is larger than that of the red curve, suggesting that the linear and nonlinear correlation is better when the 5 kHz NB emission lags the type 2 ENA injection than the other way around.

MI of two variables x and y, MI(x, y), gives a measure of the amount of information that x and y share. The amount of information is measured using Shannon entropy (Li 1990; Tsonis 2001). If x and y are completely independent, then the MI(x, y) = 0. So, in this case, MI = 0 has the same connotation as correlation coefficient r = 0. However, unlike r, which has a maximum value of one, the maximum value of MI would depend on the variables. The maximum MI is attained if we have a situation in which knowing a particular value of x would completely determine the value of y and vice versa. In this case, the maximum value of MI is the amount of information contained in x or y (entropy of y).

In order to get a measure of the significance of the MI, we calculate the mean and standard deviation (σ) from the surrogate data. We calculate noise = MI[sur(ENA) \rightarrow NB] where sur(ENA) is the surrogate data of ENA, which is

obtained by randomly permuting the order of the time series array ENA(t). The mean and standard deviation of the noise are calculated from an ensemble of 100 random permutations of MI[sur(ENA) \rightarrow NB]. The MI of these 100 surrogate data have roughly Gaussian distributions. The mean noise and 3σ from the mean noise are plotted with solid and dashed green curves, respectively, in Figure 7. In all cases, both the blue and red curves in Figure 7 are orders of magnitude larger than 3σ and, hence, are significant. For example, the peak of MI(ENA \rightarrow NB) (blue curve) in Figure 7(d) is 176σ from the mean noise and, hence, is significant. The broad peak of the blue curve suggests that the 5 kHz NB lags the type 2 injection by a few minutes to 2 hr.

5. Discussion and Summary

5.1. The Triggering of the 5 kHz NB Emission

We examine the relationship of INCA type 2 ENA sudden brightening or injection with Kronian NB emissions at 5, 10, and 20–30 kHz. Although the ENA injection is correlated with all of these waves, the best correlation is found with the 5 kHz NB. For example, for the 2009 April 22 event (event #9 in Table 1), the best cross-correlations between the type 2 ENA injection and (5, 10, and 20–30 kHz) have coefficients r=(0.70, 0.08, and 0.10), respectively (only the correlation with the 5 kHz is significant at p<0.01). The ensemble cross-correlations (of the selected eight events) for the same quantities result in r=(0.42, 0.21, and 0.32), respectively. The correlations are significant (n=1937; p<0.01) for all three cases. Wang et al. (2010) found that the NB emission

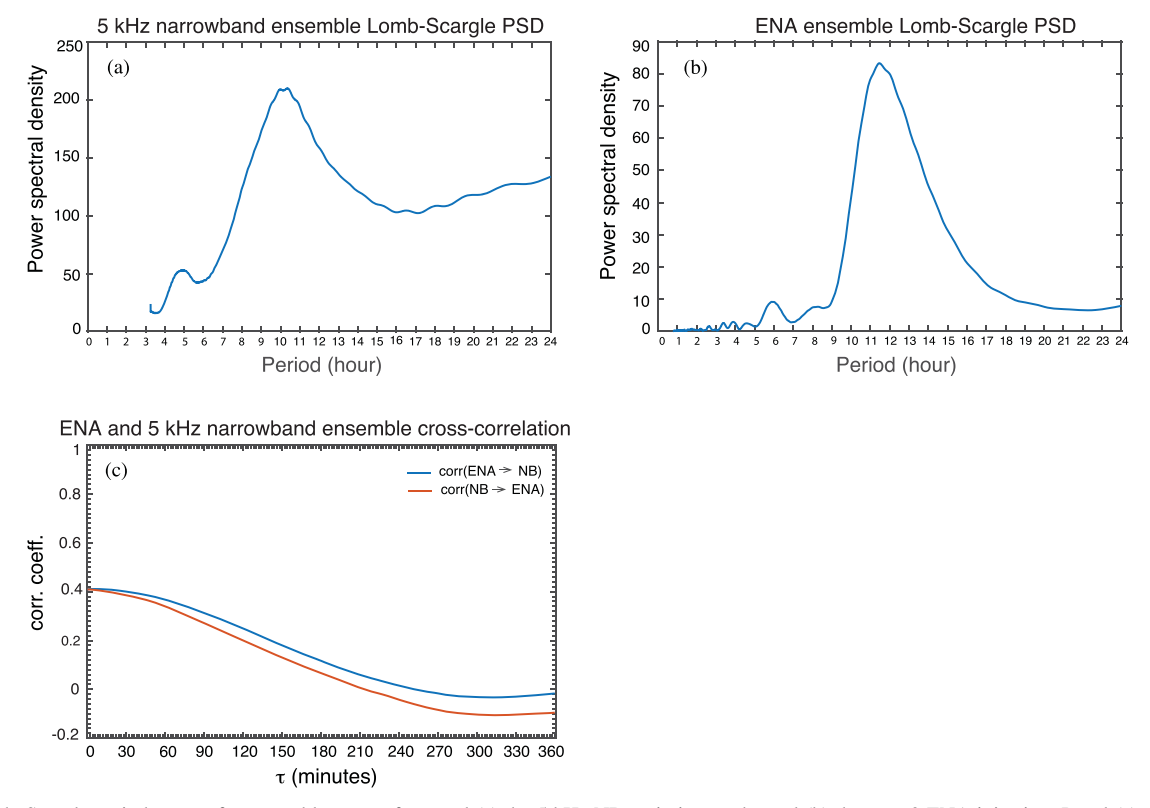


Figure 6. Lomb–Scargle periodograms for ensemble events for panel (a) the 5 kHz NB emission, and panel (b) the type 2 ENA injection. Panel (c) shows the time-shifted correlations for the ensemble events: $corr(ENA(t), NB(t + \tau))$ (ENA \rightarrow NB, blue curve) and $corr(ENA(t + \tau), NB(t))$ (NB \rightarrow ENA, red curve).

behaves like a flashing light rather than a rotating beacon, suggesting that it is triggered like SKR.

Several mechanisms have been proposed for the 5 kHz NB radio emission generation. Some of these mechanisms involve upper hybrid waves that would mode convert to O mode in a linear or nonlinear mechanism. In the linear mechanism, upper hybrid waves refract in a steep density gradient to Z-mode waves and then mode convert to O mode waves (Jones 1988; Horne 1989, 1990), and the 5 kHz NB is an O mode emission (Ye et al. 2009). In the nonlinear mechanism, upper hybrid waves coalesce with some lower-frequency waves or scatter off density irregularities to reach the free space mode (Melrose 1981; Wang et al. 2010). Menietti et al. (2009) suggested that a loss cone distribution via cyclotron maser instability can generate Z-mode waves, which can then mode convert to O mode when there is a sharp density gradient. Ye et al. (2010b) suggested that the 5 kHz NB waves are mode converted from Z-mode waves detected in the low-density region inward of the plasma torus or the orbit of Enceladus ($\sim 4 R_s$) where the ratio of electron plasma frequency to cyclotron frequency is less than unity $(f_{pe}/f_{ce} < 1)$. They hypothesized that the Z-mode waves could be excited by cyclotron maser instability when the local upper hybrid frequency is close to the harmonics of local electron cyclotron frequency.

More recently, Menietti et al. (2016) surveyed RPWS data and concluded that Z-mode waves are driven by an electron temperature anisotropy near the equator at the outer edge of the Enceladus density torus where $\omega_{\rm pe}/\Omega_{\rm ce}\leqslant 0.3$ and $T_\perp/T_\parallel>1$, where $\omega_{\rm pe}=2\pi\times$ electron plasma frequency and $\Omega{\rm ce}=2\pi\times$ electron cyclotron frequency, T_\perp = electron perpendicular temperature, and T_\parallel = electron parallel temperature. However, the source of the electron temperature anisotropy is not entirely clear in their study. One suggestion for a possible source of the

electron temperature anisotropy is the damping of ion cyclotron waves (Menietti et al. 2009).

Wang et al. (2010) examined 23 events in which the 5 kHz NB is observed by RPWS and INCA data are available. Out of those 23 events, only one event has no observation of an intense hot plasma cloud; but for this event, INCA did not point to Saturn the whole time. Thus, virtually all NB events have accompanying ENA hot plasma clouds. However, only 5 out of the 23 events (22%) show simultaneous intensifications of ENA hot plasma clouds/injections and 5 kHz NBs. They suggested that after the initial injections, the hot plasma clouds would corotate and trigger the NB emissions when they pass through certain local time. In this scenario, the phase relation between the ENA injections (sudden brightening) and 5 kHz NB intensifications can be variable or random, as their observations suggest.

However, Wang et al. (2010) did not distinguish type 1 from type 2 ENA injections and vice versa (such distinction had not yet been reported in 2010). Also, they did not quantify what "simultaneous" means, probably because of the coarse time resolution used in their study. In the example that Wang et al. (2010) presented, the NB spectrograms and ENA images span over 8 days, which makes it hard to determine the precise Δt between ENA injections and NB emission intensifications.

The present study differs from the Wang et al. (2010) study in one key aspect. We distinguish type 1 from type 2 ENA injections. Our observations suggest that there is a phase relation between type 2 ENA injections and the 5 kHz NBs. The cross-correlation of the type 2 injections and 5 kHz NBs of the ensemble events shows that the 5 kHz NB lags type 2 injection by 7 minutes (Figure 6(c)). However, the cross-correlation only captures linear correlation. The MI, which captures linear and nonlinear correlations, shows that the 5 kHz

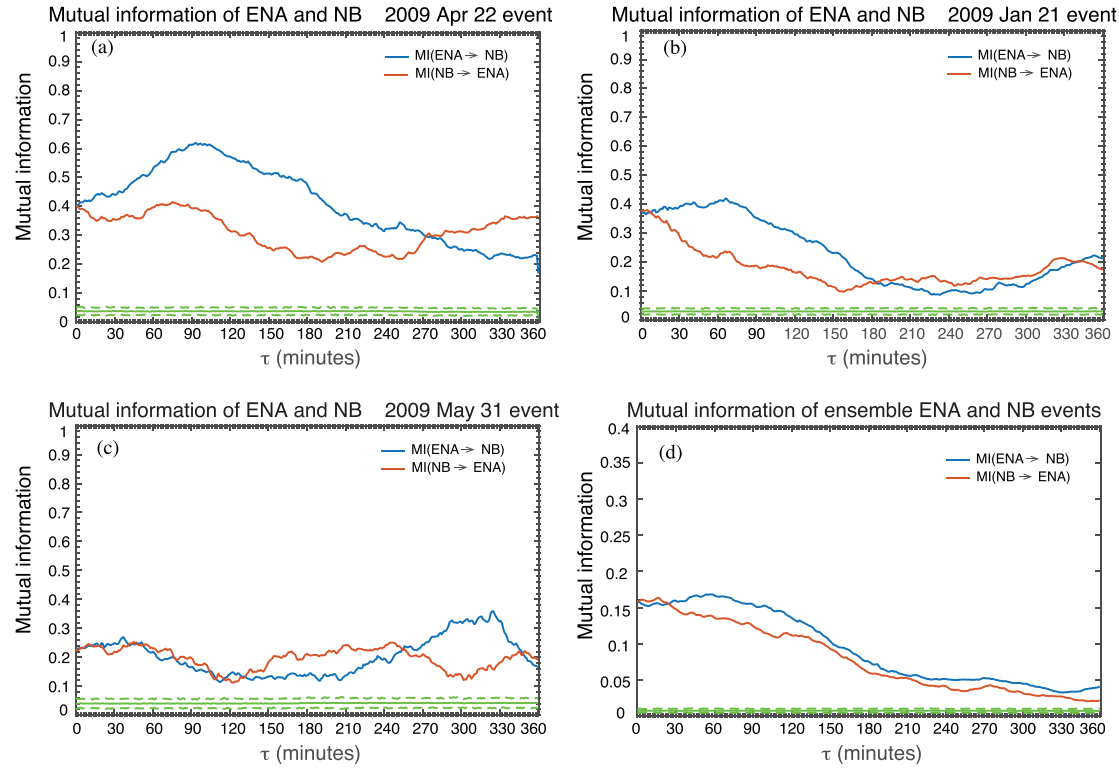


Figure 7. Panels (a), (b), (c), and (d) show MI for the 2009 April 22, 2009 January 21, 2009 March 31, and ensemble events, respectively. MI(ENA(t), NB(t) is plotted in blue while MI(ENA(t + τ), NB(t) is plotted in red. Panels (a), (b), (c), and (d) can be compared with their cross-correlation counterparts in Figures 3(d), 4(d), 5(d), and 6(c), respectively. The solid green curve is the mean noise obtained from the surrogate data, and the dashed green curve is 3 σ from the mean noise.

NB lags type 2 injection by a few minutes to 2 hr (Figure 7(d)). This timescale seems to better describe the variability seen in the individual events (see, e.g., Figures 3–5) than the timescale obtained from the cross-correlation. Although Figure 4 shows that the ENA and NB curves peak simultaneously within a window of <10 minutes, most events have larger lag times.

The variability of the lag time may be attributed to the position of the spacecraft relative to the injection. For example, the study does not take into account the ENA brightness modulation due to the ENA source moving toward or away from the spacecraft (Mitchell et al. 2004). Also, the ENA and the waves may travel on different paths to reach the spacecraft. The ENA would travel along a straight line from the injection location to the spacecraft. However, the upper hybrid waves may preferentially travel perpendicular to the magnetic field in the equatorial region (Barbosa & Kurth 1990). The 5 kHz NB waves would be launched more or less perpendicular to the density gradient at the source and may propagate in a beam-like fashion to the northern and southern hemisphere (Jones 1987). The ENA may be generated where the interchange and charge exchange occur. However, the strong upper hybrid wave growth may not occur until the injection reaches a region that is favorable for strong wave growth, and the 5 kHz may not be generated until the upper hybrid waves reach the high-density gradient region where they mode convert to Z mode and then to O mode. These may introduce variability in the lag time.

The MI analysis shows that the 5 kHz NB emission lags type 2 injection by a few minutes to 2 hr (Figure 7), which would be consistent with a scenario in which the type 2 injection can lead to 5 kHz emission. The plasma injections from the outer or middle magnetosphere would bring the hot plasma into the colder inner magnetosphere region. The electrostatic upper

hybrid waves can be generated by the electron temperature anisotropy-driven instability where there is a mixing of hot and cold electrons, gentle loss cone distribution, and "reasonable" ratio of n_c/n_h ($\lesssim 3-5$), where $n_c = \text{cold component density}$ and $n_h = \text{hot}$ component density (Hubbard & Birmingham 1978; Rönnmark et al. 1978; Wang et al. 2010). The injected hot plasma clouds would have hot electrons with a loss cone distribution that can provide the free energy that can drive the electrostatic upper hybrid waves (Menietti et al. 2009). Upper hybrid waves have been previously associated with plasma injections (Kennelly et al. 2013). When the upper hybrid waves encounter a sharp density gradient at the outer edge of the Enceladus density torus, they would mode convert to Z mode and then to O mode as mentioned above or convert to O mode directly (Melrose 1981; Jones 1988; Horne 1989, 1990; Ye et al. 2009; Menietti et al. 2016). This scenario may be consistent with the observations that place O mode wave generation around $L = 7.4 R_s$ (Wang et al. 2010).

The plasma injections also bring hot ions into the inner magnetosphere, which can generate lower hybrid and whistler mode chorus waves. These waves would pitch angle scatter the hot ions into the ionosphere, reducing the ion temperature anisotropy and the ENA emission. Thus, another possible explanation for the broad peak of the blue curve in Figure 7(d) is that the width of the peak, which is approximately 2 hr, may give a measure of the timescale for the decay of the temperature anisotropy and the pitch angle scattering rate.

However, the red curve in Figure 7(d) shows that MI(ENA $(t + \tau)$, NB(t)) is significant (as described in Section 4), suggesting that there is also a correlation with lag times in the opposite direction. After the type 2 injection, the hot plasma (ions and electrons) would corotate with the planet. As it does,

the upper hybrid waves, as proxied by the 5 kHz NB emission, would lower the electron temperature anisotropy while the lower hybrid and whistler mode chorus waves would lower the ion temperature anisotropy, decreasing the ENA emission. Thus, the good correlation shown by the red curves may result from the correlation between the 5 kHz NB emission and the lower hybrid and whistler mode chorus waves, which would decrease the ENA emission.

In some cases, the NB peaks before the ENA. It is not clear what causes this. This may be related to the viewing geometry. NB may peak before ENA because the ENA would not be visible from high latitudes (latitudes >35°) until the extreme pancake distribution of the ions has scattered to attain a more isotropic distribution. If this takes some time, the ENA would lag. Also, the local time from which INCA views the injection can result in an apparent lag in the peak ENA intensity, e.g., the blob initially moves away from the spacecraft and then later toward the spacecraft. Another possibility is that there may be simultaneous injections at more than one location. There may be a primary brightening near midnight at 21-03 MLT where the keogram is constructed, but additionally, there may be another brightening, albeit a weaker one at another location that is outside of 21-03 MLT. As an example, in one event (event #8 in Table 1), two brightening/injections appear simultaneously, one around midnight and one at postmidnight near dawn. Both have strong ENA emissions. Because of these two simultaneous injections, the periodicity deviates from the norm. Hence, the event is not included in our ensemble events.

It should be noted that the relationship between ENA injection and the 5 kHz NB emission described above is established for strong NB events (the 5 kHz NB electric field PSD $\gtrsim 10^{-14}~V^2~m^{-2}$ Hz). When the 5 kHz has weaker emission (events #4, 5, and 13 in Table 1), the response of the 5 kHz NB to type 2 ENA injection has a different characteristic. For example, the cross-correlations are weaker and the lag times between the NB and ENA peaks are larger than 2 hr. This is the subject of our follow-up study.

5.2. Periodicities of the 5 kHz NB Emission and Type 2 ENA Injection

The intensities of the 5 kHz NB and SKR emissions have been observed to have a periodicity of about 10.8 hr (Gurnett et al. 2005; Wang et al. 2010). The Lomb–Scargle analysis of the ensemble events shows that the 5 kHz NB has a periodicity of 10–11 hr (Figure 6(a)), which is consistent with the previously reported value.

The Lomb–Scargle analysis of the ensemble events shows that the ENA type 2 injection has a periodicity of 11– $12\,hr$, which is similar to the periodicity of $11.7\pm2.4\,hr$ for the H 20–50 keV obtained for the ENA injection reported by Carbary et al. (2008a). Their study did not distinguish type 1 from type 2 ENA injections. Taken together, Carbary et al. (2008a) and the present study would suggest that the periodicities of type 1 injections ($r>9\,R_{\rm s}$) and type 2 injections ($5\,R_{\rm s}< r<9\,R_{\rm s}$ in the present study) are similar. Carbary et al. (2008a) used H ENA with slightly lower energy, 20–50 keV, than 55–90 keV used in the present study, but this slight energy difference apparently does not make a significant difference in the periodicity. The periodicity of the type 2 ENA injections would be relevant to the flux tube interchange injection dynamics in the inner magnetosphere (Azari et al. 2019).

It is not clear why the type 2 ENA injection periodicity is slightly larger than the 10–11 hr periodicity seen in the 5 kHz NB waves. Previous studies have reported that the plasma corotational speed decreases with increasing distance (Achilleos et al. 2015). Our study uses only eight events, and it is not clear if using a larger number of events would give a different result (we start out with 13 events, but five events are deemed unsuitable for the analysis for the reasons listed in Table 1). However, as mentioned above, our periodicities for ENA and NB emissions seem to be consistent with previous studies that used larger data sets (Carbary et al. 2008a; Wang et al. 2010). Another possibility is that the injected plasma blob may not completely decay in one revolution, although most do. The old plasma blobs that do not completely decay in one revolution may contaminate the intensity of the next fresh injection in the keogram at 21-03 MLT. The O ENA is much better behaved than the H ENA, in that its emission both grows and decays much more quickly than the H ENA. For example, Carbary et al. (2008a) reported a periodicity of $10.8 \pm 0.2 \,\mathrm{hr}$ for O ENA. However, the disadvantage of using O ENA is that the O fluxes are typically lower than H fluxes, which would introduce counting statistics problems in some cases. The present study chooses H with energy 55-90 keV over 20-50 keV because the higher-energy H may decay faster than the lower-energy H; but as discussed above, this energy difference does not seem to change the periodicity significantly. Another possibility is that a small fresh injection may occur outside the 21-03 MLT, which may perturb the periodicity.

5.3. Broader Implications for Jupiter and Brown Dwarfs

As pointed out by Louarn et al. (2007), the occurrence pattern of SKR and NB emissions observed at Saturn (Figure 2) has striking similarities with the Jovian Hectometric (HOM) and NB (n-KOM) radio emission patterns. Other than Cassini's flyby of Jupiter at the end of 2000 (Mauk et al. 2003; Mitchell et al. 2004), no dedicated ENA imaging has been carried out at Jupiter that could diagnose the large-scale injection patterns of energetic ions. The next mission to do so is the Jupiter Icy Moon Explorer that carries the Jovian Energetic Neutrals and Ion Camera (Mitchell et al. 2016). However, the strikingly similar patterns of periodic radio emissions of Jupiter strongly imply that the underlying magnetospheric injections may be of the same nature as the ones observed by INCA at Saturn. In situ measurements by the Galileo mission have revealed quasiperiodic radial flow bursts in the postmidnight sector (Krupp et al. 1998; Woch et al. 2002; Kronberg et al. 2007, 2005), not unlike the ones observed at Saturn.

At Earth, it is well known that the AKR correlate highly with auroral substorm and injections (Liou et al. 2000). AKR is observed in the 30–800 kHz range and has a source altitude of 1–3 $R_{\rm e}$ ($R_{\rm e}$ = radius of the Earth = 6371 km) in the premidnight sector. Terrestrial substorms are associated with large-scale particle injections in the midnight sector, as shown by multiple missions and observed remotely in ENAs by, for example, the IMAGE mission (Mitchell et al. 2003).

Hallinan et al. (2015) reported simultaneous radio and optical observations of the brown dwarf star LSR J18351 +3259 that show periodicities in both wavelengths at the rotational periodicity of 2.84 hr as determined through using the Karl G. Jansky Very Large Array at radio wavelengths, along with the 5 m Hale Telescope on Palomar Mountain and the 10 m Keck Telescope in Hawaii at optical wavelengths,

strongly implying a magnetospheric current system driving electron precipitation that in turn generates radio and auroral emissions. Our results here, together with the observations of the highly correlated auroral emissions at Saturn, strongly suggest that magnetospheric processes, such as large-scale injections, seem to be a universal process that are at work even at brown dwarfs. We suggest that the FAC systems set up by the plasma pressure gradients of the injected ion populations may directly drive the radio emissions through a cyclotron maser instability (Hallinan et al. 2008). The present study suggests that it may also be possible that the injection of hot electrons into the cold plasma environment, e.g., the inner magnetosphere, and the resulting temperature anisotropy can lead to the growth of the electrostatic upper hybrid waves and NB radio wave emissions at astrophysical objects, albeit such emissions may be weaker than the ones caused by the electron cyclotron maser instability. In any case, injections would constitute the engine behind periodic radio wave emissions across a range of magnetized objects. However, the underlying cause of the periodic behavior of all of these phenomena still remains a mystery, but it is likely driven by the fast rotation of the objects.

6. Conclusion

The relationship between ENA type 2 injections with the $5\,\mathrm{kHz}$ NB emissions for strong NB events (electric field PSD $>\sim 10^{-14}~\mathrm{V^2~m^{-2}~Hz}$) is examined in eight events. The phase relation between the ENA injection and the NB emission is not random. The MI analysis shows that the $5\,\mathrm{kHz}$ NB emission lags type 2 ENA injection by a few minutes to 2 hr, which would be consistent with a scenario in which the type 2 injection can cause the $5\,\mathrm{kHz}$ NB emission. The injection of hot plasma into the inner magnetosphere can result in electron temperature anisotropy. Previous studies suggested that temperature anisotropy can generate electrostatic upper hybrid waves, which, upon encountering the high-density gradient at the outer edge of the Enceladus density torus, can mode convert to Z mode, which can then mode convert to O mode. The $5\,\mathrm{kHz}$ NB commonly propagates in the O mode.

Once the injected flux tube reaches the inner magnetosphere, it corotates with the planet. As it does, it continues to generate upper hybrid waves and the 5 kHz NB emission as well as lower hybrid and whistler mode chorus waves. These waves would reduce the electron and ion temperature anisotropy, which would in turn reduce the wave growth. Thus, the 5 kHz emission and the type 2 ENA emissions would decrease over time as the hot plasma blob corotates with the planet.

A key to establishing the relationship between the ENA injections and the Kronian waves is recognizing that there are two types of ENA injections. Only type 2 injections have a causal relationship with the 5 kHz NB emission. Previous studies that did not distinguish between the two types of ENA injections found that there is no phase relation between ENA injections and the 5 kHz NB emissions (Wang et al. 2010) and SKR (Carbary et al. 2010).

It should be noted when the 5 kHz NB has weaker emissions (electric field PSD $\lesssim 10^{-14}~V^2~m^{-2}~Hz$) as seen in events #4, 5, and 13 in Table 1, the response of the 5 kHz NB to the type 2 ENA injection has a different characteristic. For example, the cross-correlations are weaker, and the lag times between the NB and ENA peaks are larger than 2 hr. This is the subject of our follow-up study.

Finally, the 11-12 hr periodicity of the type 2 ENA injection is similar to the 11.7 ± 2.4 hr periodicity of ENA injection obtained by Carbary et al. (2008a). Carbary et al. (2008a) did not distinguish between type 1 from type 2 injections. Thus, taken together, this would suggest that the periodicities of type 1 and type 2 injections are similar.

All of the derived data products in this paper are available upon request by email to the lead author (simon.wing@jhuapl.edu). Cassini RPWS data are archived at the NASA Planetary Data System (PDS) website (https://pds-ppi.igpp.ucla.edu/search/ view/?f=yes&id=pds://PPI/CO-S-MIMI-4-INCA-CALIB-V1.0). Cassini INCA data are available at the PDS: Plasma Interaction website (https://pds-ppi.igpp.ucla.edu/search/ view/?f=yes&id=pds://PPI/CO-S-MIMI-4-INCA-CALIB-V1.0) and its mirror site at JHU/APL (http://cassini-mimi. jhuapl.edu/PDS Volumes/COMIMI I001/DATA/). We thank Hari Nair and Martha Kusterer for providing the Cassini software tools for data visualization and analysis. The research at the Johns Hopkins University Applied Physics Laboratory was supported by the NASA Office of Space Science under Task Order 003 of contract NAS5-97271 between NASA Goddard Space Flight Center and the Johns Hopkins University and NASA grants (NNX12AG81G, NNX15AJ01G, and NNX16AQ87G, 80NSSC19K0822). The research at Andrews University was supported by NASA grants (NNX16AQ876, 80NSSC19k0843), and NSF grants (AGS1532207, AGS1602855), and Andrews University Faculty Research Grant. The research at the University of Iowa was supported by NASA through contract 1415150 with the Jet Propulsion Laboratory and NASA grant NNX16AI47G.

ORCID iDs

S. Wing https://orcid.org/0000-0001-9342-1813

D. G. Mitchell https://orcid.org/0000-0003-1960-2119

References

```
Achilleos, N., André, N., Blanco-Cano, X., et al. 2015, SSRv, 187, 229
Azari, A. R., Jia, X., Liemohn, M. W., et al. 2019, JGRA, 124, 1806
Azari, A. R., Liemohn, M. W., Jia, X., et al. 2018, JGRA, 123, 4692
Barbosa, D. D., & Kurth, W. S. 1990, JGR, 95, 8177
Birn, J., Hesse, M., Schindler, K., & Zaharia, S. 2009, JGR, 114, A00D03
Bradley, T. J., Cowley, S. W. H., Bunce, E. J., et al. 2018, JGRA, 123, 9476
Carbary, J. F., Krimigis, S. M., Mitchell, D. G., Paranicas, C., & Brandt, P.
  2009, AdSpR, 44, 483
Carbary, J. F., & Mitchell, D. G. 2014, JGRA, 119, 1771
Carbary, J. F., Mitchell, D. G., Brandt, P., Paranicas, C., & Krimigis, S. M.
  2008a, GeoRL, 35, L07102
Carbary, J. F., Mitchell, D. G., Brandt, P., Roelof, E. C., & Krimigis, S. M.
  2008b, JGR, 113, A05210
Carbary, J. F., Mitchell, D. G., Krimigis, S. M., Gurnett, D. A., & Kurth, W. S.
  2010, JGR, 115, A01203
Chen, Y., & Hill, T. W. 2008, JGR, 113, A07215
Darbellay, G. A., & Vajda, I. 1999, ITIT, 45, 1315
Davies, M. E., Abalakin, V. K., Bursa, M., et al. 1995, CeMDA, 63, 127
De Michelis, P., Consolini, G., Materassi, M., & Tozzi, R. 2011, JGR, 116,
   A08225
De Michelis, P., Tozzi, R., & Consolini, G. 2017, EP&S, 69, 24
Eather, R. H. 1984, JGR, 89, 1695
Ergun, R. E., Carlson, C. W., McFadden, J. P., et al. 2000, ApJ, 538, 456
Gurnett, D. A. 1974, JGR, 79, 4227
Gurnett, D. A., Kurth, W. S., Hospodarsky, G. B., et al. 2005, Sci, 307, 1255
Gurnett, D. A., Kurth, W. S., Kirchner, D. L., et al. 2004, SSRv, 114, 395
Gurnett, D. A., Kurth, W. S., & Scarf, F. L. 1981, Natur, 292, 733
Hallinan, G., Littlefair, S. P., Cotter, G., et al. 2015, Natur, 523, 568
Hallinan, G., Antonova, A., Doyle, J. G., et al. 2008, ApJ, 684, 644
Horne, R. B. 1989, JGR, 94, 8895
Horne, R. B. 1990, JGR, 95, 3925
```

```
Hubbard, R. F., & Birmingham, T. J. 1978, JGR, 83, 4837
Jackman, C. M., Achilleos, N., Cowley, S. W. H., et al. 2013, P&SS, 82, 34
Johnson, J. R., & Wing, S. 2009, JGRA, 114, A00D08
Johnson, R. E., Smith, H. T., Tucker, O. J., et al. 2006, ApJL, 644, L137
Jones, D. 1987, Natur, 327, 492
Jones, D. 1988, in Planetary Radio Emissions II, ed. H. O. Rucker,
   S. J. Bauer, & B. M. Pedersen (Vienna: Austrian Acad. of Sci. Press), 245
Kennelly, T. J., Leisner, J. S., Hospodarsky, G. B., & Gurnett, D. A. 2013,
   JGRA, 118, 832
Krimigis, S. M., Mitchell, D. G., Hamilton, D. C., et al. 2004, SSRv, 114, 233
Krimigis, S. M., Mitchell, D. G., Hamilton, D. C., et al. 2005, Sci, 307, 1270
Kronberg, E. A., Glassmeier, K.-H., Woch, J., et al. 2007, JGR, 112, A05203
Kronberg, E. A., Woch, J., Krupp, N., et al. 2005, JGR, 110, A03211
Krupp, N., Woch, J., Lagg, A., et al. 1998, GeoRL, 25, 1249
Kurth, W. S., Lecacheux, A., Averkamp, T. F., Groene, J. B., & Gurnett, D. A.
   2007, GeoRL, 34, L02201
Kurth, W. S., Bunce, E. J., Clarke, J. T., et al. 2009, in Saturn From Cassini-
   Huygens, ed. M. K. Dougherty, L. W. Esposito, & S. M. Krimigis (New
   York: Springer), 333
Lamy, L., Prangé, R., Pryor, W., et al. 2013, JGRA, 118, 4817
Lamy, L., Schippers, P., Zarka, P., et al. 2010, GeoRL, 37, L12104
Lamy, L., Zarka, P., Cecconi, B., et al. 2008, JGR, 113, A07201
Li, W. 1990, JSP, 60, 823
Liou, K., Meng, C.-I., Lui, A. T. Y., Newell, P. T., & Anderson, R. R. 2000,
   IGR, 105, 25325
Louarn, P., Kurth, W. S., Gurnett, D. A., et al. 2007, GeoRL, 34, L20113
March, T. K., Chapman, S. C., & Dendy, R. O. 2005, GeoRL, 32, L04101
Materassi, M., Ciraolo, L., Consolini, G., & Smith, N. 2011, AdSpR, 47, 877
Mauk, B. H., Mitchell, D. G., Krimigis, S. M., Roelof, E. C., & Paranicas, C. P.
   2003, Natur, 421, 920
Melrose, D. B. 1981, JGR, 86, 30
Menietti, J. D., Ye, S.-Y., Yoon, P. H., et al. 2009, JGR, 114, A06206
Menietti, J. D., Yoon, P. H., Písa, D., et al. 2016, JGRA, 121, 11929
Mitchell, D. G., Brandt, P. C., Carbary, J. F., et al. 2015, in Injection,
```

Interchange, and Reconnection, in Magnetotails in the Solar System, ed.

```
Sons, Inc)
Mitchell, D. G., Brandt, P. C., Roelof, E. C., et al. 2003, SSRv, 109, 63
Mitchell, D. G., Brandt, P. C., Westlake, J. H., et al. 2016, JGRA, 121, 8804
Mitchell, D. G., Brant, P. C., Roelof, E. C., et al. 2005, GeoRL, 32, L20S01
Mitchell, D. G., Krimigis, S. M., Paranicas, C., et al. 2009, P&SS, 57, 1732
Mitchell, D. G., Paranicas, C. P., Mauk, B. H., Roelof, E. C., & Krimigis, S. M.
   2004, JGRA, 109, A09S11
Nakamura, R., Baumjohann, W., Brittmacher, M., et al. 2001, JGR, 106,
  10777
Paranicas, C., Mitchell, D. G., Roelof, E. C., et al. 2005, GeoRL, 32, L21101
Persoon, A. M., Gurnett, D. A., Leisner, J. S., et al. 2013, JGRA, 118, 2970
Radioti, A., Roussos, E., Grodent, D., et al. 2013, JGRA, 118, 1922
Rairden, R. L., & Mende, S. B. 1989, JGR, 94, 1402
Rönnmark, K., Borg, H., Christiansen, P. J., Gough, M. P., & Jones, D. 1978,
   SSRv, 22, 401
Sergeev, V. A., Liou, K., Newell, P. T., et al. 2004, AnGeo, 22, 537
Thomsen, M. F. 2013, GeoRL, 40, 5337
Thomsen, M. F., Mitchell, D. G., Jia, X., et al. 2015, JGRA, 120, 2571
Tsonis, A. A. 2001, NPGeo, 8, 341
Wang, Z., Gurnett, D. A., Fischer, G., et al. 2010, JGR, 115, A06213
Wing, S., & Johnson, J. R. 2009, JGR, 114, A00D07
Wing, S., & Johnson, J. R. 2010, JGR, 115, A00D00
Wing, S., & Johnson, J. R. 2019, Entrp, 21, 140
Wing, S., Johnson, J. R., Camporeale, E., & Reeves, G. D. 2016, JGRA,
   121, 9378
Wing, S., Johnson, J. R., Chaston, C. C., et al. 2014, SSRv, 184, 33
Woch, J., Krupp, N., & Lagg, A. 2002, GeoRL, 29, 1138
Wolf, R. A., Wan, Y., Xing, X., Zhang, J.-C., & Sazykin, S. 2009, JGRA, 114,
   A00D05
Wu, C. S., & Lee, L. C. 1979, ApJ, 230, 621
Ye, S.-Y., Gurnett, D. A., Fischer, G., et al. 2009, JGR, 114, A06219
Ye, S.-Y., Gurnett, D. A., Groene, J. B., Wang, Z., & Kurth, W. S. 2010a, JGR,
Ye, S.-Y., Menietti, J. D., Fischer, G., et al. 2010b, JGR, 115, A08228
```

A. Keiling, C. M. Jackman, & P. A. Delamere (Hoboken, NJ: John Wiley &